ORIGINAL ARTICLE

MATR3 disruption in human and mouse associated with bicuspid aortic valve, aortic coarctation and patent ductus arteriosus

Fabiola Quintero-Rivera[1,2,†], Qiongchao J. Xi[3,†], Kim M. Keppler-Noreuil[5,‡],
Ji Hyun Lee[1,¶], Anne W. Higgins[4,§], Raymond M. Anchan[3,4], Amy E. Roberts[6,7],
Ihn Sik Seong[1], Xueping Fan[8], Kasper Lage[9], Lily Y. Lu[3], Joanna Tao[3],
Xuchen Hu[3], Ronald Berezney[10], Bruce D. Gelb[11], Anna Kamp[12,‖],
Ivan P. Moskowitz[12], Ronald V. Lacro[6], Weining Lu[8], Cynthia C. Morton[4,13],
James F. Gusella[1,*] and Richard L. Maas[3,*]

[1]Molecular Neurogenetics Unit and Center for Human Genetic Research, Massachusetts General Hospital and Harvard Medical School, Boston, MA, USA, [2]Department of Pathology and Laboratory Medicine, David Geffen School of Medicine at UCLA, Los Angeles, CA, USA, [3]Division of Genetics, Department of Medicine, [4]Department of Obstetrics, Gynecology and Reproductive Medicine, Brigham and Women's Hospital and Harvard Medical School, Boston, MA, USA, [5]Division of Medical Genetics, University of Iowa Hospitals and Clinics, Iowa City, IA, USA, [6]Department of Cardiology, [7]Division of Genetics, Department of Medicine, Boston Children's Hospital and Harvard Medical School, Boston, MA, USA, [8]Renal Section, Department of Medicine, Boston University Medical Center, Boston, MA, USA, [9]Pediatric Surgical Research Laboratories, Department of Surgery, Massachusetts General Hospital for Children and Harvard Medical School, Boston, MA, USA, [10]Department of Biological Sciences, University at Buffalo, Buffalo, NY, USA, [11]Mindich Child Health and Development Institute, Departments of Pediatrics and Genetics and Genomic Sciences, Icahn School of Medicine at Mount Sinai, NY, USA, [12]Departments of Pediatrics and Pathology, University of Chicago, Chicago, IL, USA and [13]Department of Pathology, Brigham and Women's Hospital, Boston, MA, USA

*To whom correspondence should be addressed. Email: gusella@helix.mgh.harvard.edu (J.F.G.); maas@genetics.med.harvard.edu (R.L.M.)

Abstract

Cardiac left ventricular outflow tract (LVOT) defects represent a common but heterogeneous subset of congenital heart disease for which gene identification has been difficult. We describe a 46,XY,t(1;5)(p36.11;q31.2)dn translocation carrier with pervasive

developmental delay who also exhibited LVOT defects, including bicuspid aortic valve (BAV), coarctation of the aorta (CoA) and patent ductus arteriosus (PDA). The 1p breakpoint disrupts the 5′ UTR of *AHDC1*, which encodes AT-hook DNA-binding motif containing-1 protein, and *AHDC1*-truncating mutations have recently been described in a syndrome that includes developmental delay, but not congenital heart disease [Xia, F., Bainbridge, M.N., Tan, T.Y., Wangler, M.F., Scheuerle, A.E., Zackai, E.H., Harr, M.H., Sutton, V.R., Nalam, R.L., Zhu, W. *et al.* (2014) *De Novo* truncating mutations in AHDC1 in individuals with syndromic expressive language delay, hypotonia, and sleep apnea. *Am. J. Hum. Genet.*, 94, 784–789]. On the other hand, the 5q translocation breakpoint disrupts the 3′ UTR of *MATR3*, which encodes the nuclear matrix protein Matrin 3, and mouse *Matr3* is strongly expressed in neural crest, developing heart and great vessels, whereas *Ahdc1* is not. To further establish *MATR3* 3′ UTR disruption as the cause of the proband's LVOT defects, we prepared a mouse *Matr3*^Gt-ex13 gene trap allele that disrupted the 3′ portion of the gene. *Matr3*^Gt-ex13 homozygotes are early embryo lethal, but *Matr3*^Gt-ex13 heterozygotes exhibit incompletely penetrant BAV, CoA and PDA phenotypes similar to those in the human proband, as well as ventricular septal defect (VSD) and double-outlet right ventricle (DORV). Both the human *MATR3* translocation breakpoint and the mouse *Matr3*^Gt-ex13 gene trap insertion disturb the polyadenylation of *MATR3* transcripts and alter Matrin 3 protein expression, quantitatively or qualitatively. Thus, subtle perturbations in Matrin 3 expression appear to cause similar LVOT defects in human and mouse.

Introduction

Congenital heart defects (CHDs) are the most common human birth defects, affecting nearly 1 per 100 liveborn infants, and a leading cause of infant mortality [reviewed in (1,2)]. The etiology for most of these defects is unknown, but both environmental and genetic factors are likely to be contributory (3,4). Complex genetics, combined with the traditional classification of cardiac malformations by physiology and anatomy, have made investigation of the genetic component of CHD challenging.

Left ventricular outflow tract obstruction (LVOTO) malformations comprise ~14% of CHD and consist of anatomically varied defects with a wide spectrum of clinical severity, including bicuspid aortic valve (BAV), coarctation of the aorta (CoA), hypoplastic left heart (HLH) and interrupted aortic arch (IAA) type A. BAV is the most common form of LVOTO and of CHD (5). Although generally asymptomatic, BAV constitutes an important risk factor for subacute bacterial endocarditis and, at high frequency in adults, for late onset aortic valve calcification, aortic stenosis and aortic dilatation, which frequently require valve replacement (6,7). CoA is also a common LVOTO defect, accounting for 6–8% of all CHD live births; left untreated, it frequently culminates in serious hypertension (8).

Evidence supports a strong genetic involvement in the causation of LVOTO defects, and both copy number variants and mutations in histone modifying genes have been implicated (9,10), as well as mutations in other genes. One gene implicated in human LVOTO defects is *NOTCH1* (11–14). A subset of *NOTCH1* mutations reduce Jagged-induced Notch-dependent signal transduction and lead to defective epithelial–mesenchymal transition in endothelial cells (12,13). In addition, targeted loss-of-function in mouse *Nos3*, that encodes endocardial nitric oxide synthase type 3, and in mouse and human *GATA5,* which encode a Zn-finger transcription factor, produce BAV phenotypes (15–18). Both *Nos3* and *Gata5* act in the valvular endothelium where *Gata5* appears to affect differentiation and to act upstream of *Jag1* and *Tbx20* (16). Gata5 also trans-activates the *Nos3* promoter *in vitro*, and *Gata5* interacts genetically with *Gata4* and *Gata6 in vivo* (16,19). Moreover, deficiency for the Gata co-factor Fog1 results in double-outlet right ventricle (DORV), whereas *Fog2* deficiency results in overriding aorta, subpulmonic stenosis and subaortic ventricular septal defect (VSD) (20). Interestingly, *Nos3, Gata4* and *Tbx20* are part of an endocardial pathway required for atrial septum formation (21). Another gene, *ERRB4*, which encodes a receptor tyrosine kinase for EGF ligands, is also associated with LVOTO defects and may function within this pathway (22).

Endothelial defects are especially well exemplified by loss-of-function for *Plexin D1*, which also results in LVOTO (23). Lastly, mesenchymal defects can also contribute to LVOTO, as deficiency of the Activin type I receptor Alk2 in cushion mesenchyme results in a high incidence of BAV (24,25).

A key role for neural crest involvement is suggested by DiGeorge syndrome, which involves outflow tract and aortic arch defects and most often results from deletions of 22q11 and haploinsufficiency for *TBX1*. Recent studies have identified a number of *Tbx1* co-regulatory pathways including, among others, *Six1/ Eya1* and *p53* (26,27). BAV and CoA may be developmentally and genetically related, as both phenotypes often co-occur and may result from a common mechanism involving neural crest perturbation (28). Besides the genes mentioned earlier, *Hey2* (29), *TBL1Y* (30) and *MCTP2* (31) have been associated with a predominant CoA phenotype. Patent ductus arteriosus (PDA) is frequently associated with other cardiac anomalies [reviewed in (32)], but in mouse and human, only *TFAP2B* mutations are associated with PDA as the predominant cardiac phenotype (33–35).

To identify additional genes responsible for LVOTO defects, we utilized the Developmental Genome Anatomy Project (DGAP), which uses balanced chromosomal rearrangement breakpoints to identify potential candidate genes (36). We identified and analyzed a subject, designated DGAP105, with a balanced translocation 46,XY,t(1;5)(p36.11;q31.2)dn. This proband exhibited a global delay in development with a marked delay in speech and was also given a clinical diagnosis of Noonan-like syndrome with BAV, CoA and PDA; these and other cardiac defects are present in ~50% of Noonan syndrome (NS) cases (37). However, we were unable to identify mutations in *PTPN11*, *KRAS* and *SOS1* that, collectively, account for the majority of NS (37). Therefore, we used the DGAP105 translocation breakpoints to gain insight into the proband's phenotype and identified disruptions in two genes, *MATR3* and *AHDC1*, which together account for many features of the proband's phenotype. Recent work (38) indicates that *AHDC1* loss-of-function is sufficient to account for the impaired cognitive development and pervasive development disorder of the DGAP105 proband. Furthermore, we find that *MATR3* transcripts are disturbed and that Matrin 3 protein expression is affected in DGAP105 cells and in affected heterozygous *Matr3*^GT-ex13-mutant mice. In addition, both human and mouse *MATR3* mutants exhibit similar BAV, CoA and PDA phenotypes. Collectively, these results support a role for Matrin 3 in the formation of the cardiac outflow valves and great vessels and indicate that subtle alterations in human *MATR3* can cause medically important cardiac LVOT phenotypes.

Results

DGAP105 cardiac phenotype

At birth, the proband exhibited BAV, CoA and PDA (Figure 1A–D). An echocardiogram at 2 days of age showed CoA with a posterior shelf just distal to the left subclavian artery (Fig. 1C), with turbulent flow in the descending aorta. Doppler measurements revealed a 30 mmHg peak gradient across the CoA. The transverse aortic arch between the carotid and left subclavian arteries also appeared hypoplastic and narrow with a 4.4-mm diameter for the transverse aorta compared with 5.7 mm for the ascending aorta (Fig. 1D). A BAV was present, with normal flow velocity across it. The intercoronary commissure was fused between right and left (R–L) coronary cusps, with non-fused commissures between right and non-coronary (R–N) and between left and non-coronary (L–N) cusps. Mild-to-moderate tricuspid insufficiency was also noted. The mitral valve orifice appeared small in the short axis view, but mitral inflow velocity (98 cm/s) and pressure halftime (61 ms) were normal, and the papillary muscles intact. The right ventricle and pulmonary artery appeared dilated, but a normal flow velocity was measured in the pulmonary artery. Left ventricular function and pulmonary vein drainage into the left atrium were normal. A PDA (Fig. 1C) with predominant left-to-right shunting and a small left-to-right shunt across a patent foramen ovale were present. An ECG revealed sinus rhythm with left axis deviation. The CoA was corrected surgically via end-to-end anastomosis at 3 weeks of age, and subsequent echocardiograms to 17 years of age show no evidence of aortic re-narrowing or of regurgitant flow across the BAV. Other clinical findings, including impaired development of intellectual, speech
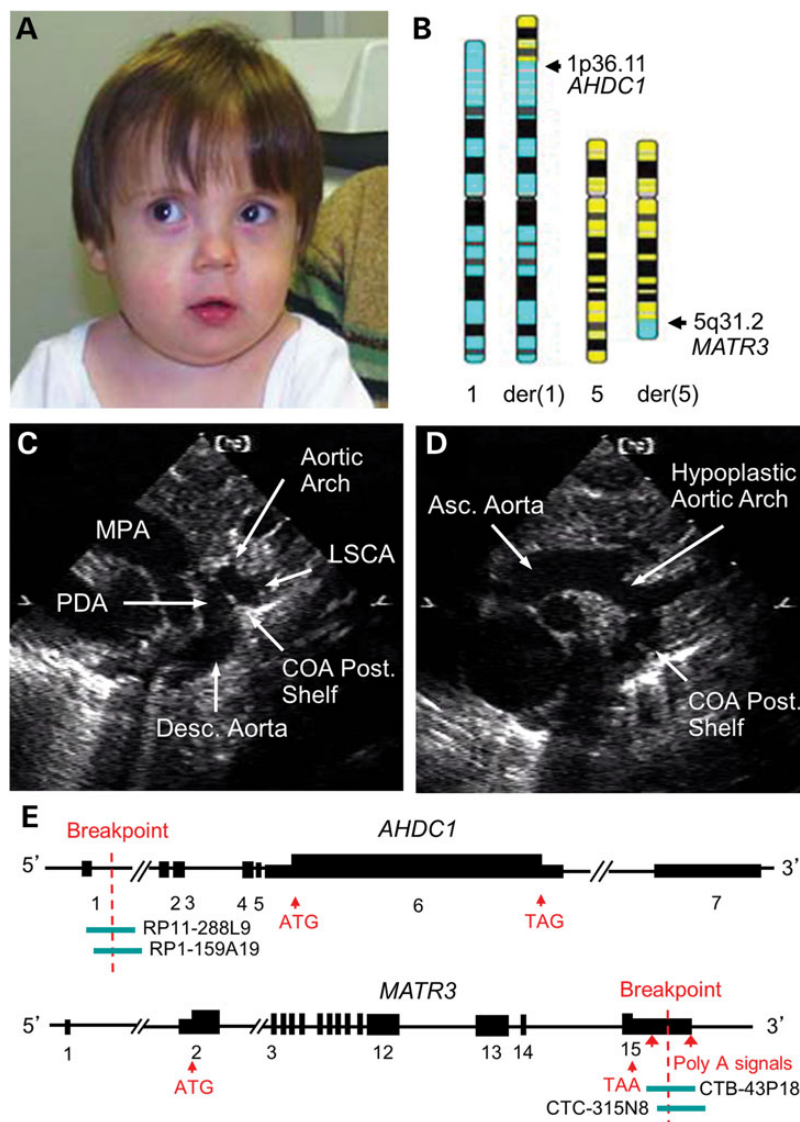

Figure 1. Clinical features, cardiac phenotype and translocation breakpoint structure in DGAP105. (**A**) Facial features at 4 years of age included mild hypertelorism, bilateral epicanthal folds, downslanting palpebral fissures, strabismus and a broad nose with a smooth philtrum and thin vermillion border. (**B**) Ideograms depicting 46,XY,t(1;5)(p36.11;q31.2)dn. Arrows mark locations of *AHDC1* and *MATR3* breakpoints. (**C** and **D**) Echocardiograms at age of 2 days. (C) Ductal view showing distal aortic arch, CoA just distal to the left subclavian artery (LSCA), accompanied by a prominent posterior unfolding ('posterior shelf') and PDA. (D) Aortic arch view showing ascending aorta (5.7-mm diameter), hypoplastic aortic arch (4.4-mm diameter) and CoA posterior shelf. (**E**) Summary of the 1p36.11 and 5q31.2 breakpoints in DGAP105. The 1p36.11 breakpoint disrupts *AHDC1* intron 1, whereas the 5q31.2 breakpoint disrupts *MATR3* exon 15 in the 3′ UTR. BACs used in FISH analyses are indicated.

and motor skills, are summarized in Supplementary Material under 'DGAP105 clinical history'.

Disruption of *MATR3* and *AHDC1* in DGAP105

Chromosomal analysis revealed a *de novo* balanced translocation that was assigned as 46,XY,t(1;5)(p36.11;q31.2)dn based on FISH mapping (Fig. 1B; Supplementary Material, Figs S1 and S2). Further FISH and Southern blot analysis localized the breakpoint region to intron 1 of *AHDC1*, encoding AT hook, DNA-binding motif containing-1 protein (Fig. 1E; Supplementary Material, Fig. S2). Amplification of the der(1) junction fragment by suppression PCR retrieved the 5q31.2 breakpoint, which was confirmed by FISH (Fig. 1E; Supplementary Material, Fig. S2). Sequence analysis of the junction fragment from the der(1) revealed an intronic 13-bp deletion of chromosome 1, whereas sequence of the fragment cloned from the der(5) showed a 3-bp insertion (Supplementary Material, Fig. S3). The 5q31.2 breakpoint occurred 667 bp downstream of the stop codon and in the 3′ UTR of *MATR3* exon 15. Thus, two distinct genes, *AHDC1* at chromosome 1p36.11 and *MATR3* at 5q31.2, are disrupted by the reciprocal translocation breakpoints in DGAP105. Array CGH at ∼9-kb resolution did not detect gain or loss of genomic sequence at the breakpoints or in the other regions of the genome.

RT–PCR showed that both *AHDC1* and *MATR3* are expressed in lymphoblasts. To further characterize the 3′ UTR of *MATR3* and the consequences of its disruption by the translocation, we performed 3′ RACE (Fig. 2A and B). 3′ RACE on control human lymphoblast and human fetal heart RNA revealed two *MATR3* 3′ RACE products of 1589 and 963 bp, each using a different AAUAAA polyadenylation signal. Lymphoblast *MATR3* transcripts predominantly employ a distal AAUAAA signal in exon 15 located 988 bp downstream of the *MATR3* stop codon (Fig. 2B). However, in human fetal heart, the predominant transcripts employ a proximal AAUAAA, located 362 bp downstream of the stop codon (Fig. 2B). This pattern of differential polyadenylation was supported by northern blot analysis of adult human tissues (Fig. 2C), which detected a 3.5-kb transcript, consistent with use of the distal polyadenylation signal in all tissues examined except for heart and skeletal muscle. In these two tissues, a shorter 2.9-kb transcript predominates, consistent with the use of the proximal polyadenylation signal (Fig. 2C).

Based on these results, the translocation breakpoint should disrupt the longer *MATR3* transcripts that employ the distal polyadenylation signal, but not the shorter transcripts that use the proximal polyadenylation signal. To test this hypothesis, we performed 3′ RACE on RNA from DGAP105 and control lymphoblasts (Fig. 2B). As expected, we observed a reduction in the levels of the longer 1589-bp product in DGAP105 lymphoblasts. Notably, however, we also observed up-regulated expression in DGAP105 lymphoblasts of the shorter 963-bp product that is normally present in fetal heart, but only at very low levels in control lymphoblasts (Fig. 2B). Thus, DGAP105 lymphoblasts exhibit reduced expression of distal polyadenylated *MATR3* transcripts but increased expression of proximal polyadenylated *MATR3* transcripts that normally predominate in human fetal heart.

These results suggest that alterations in the levels of the two *MATR3* transcript classes may be causally linked to the LVOT defects observed in the DGAP105 proband. To assess the potential impact on Matrin 3 protein levels, we performed western blot analyses on control and DGAP105 lymphoblasts (Fig. 2D and E). Using a Matrin 3-specific antibody, we detected a statistically
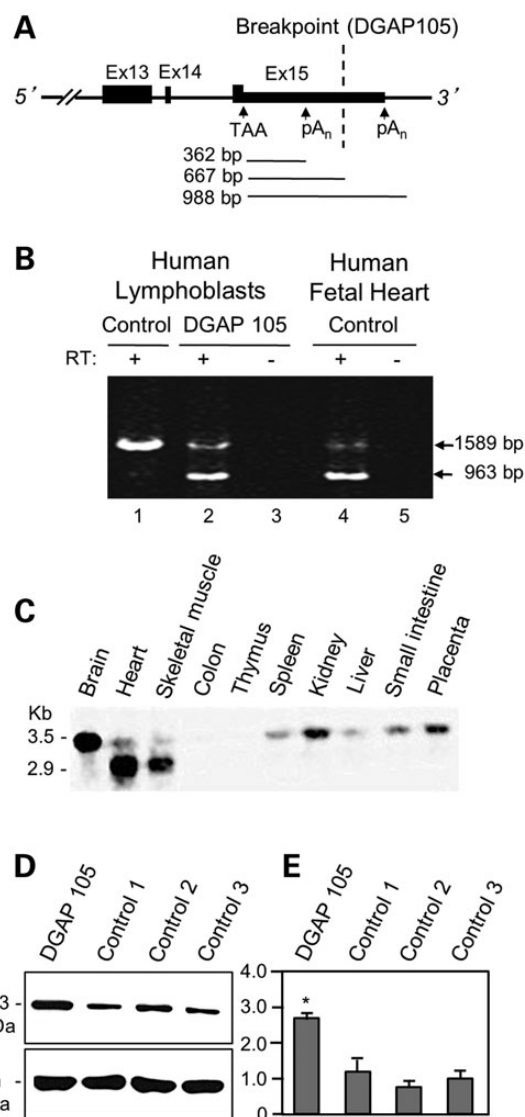

Figure 2. Analysis of human *MATR3* transcripts and protein expression in control and DGAP105 lymphoblasts. (**A**) Schematic of the *MATR3* exon 13–15 region with the chromosomal translocation breakpoint in patient DGAP105 marked by dotted line. The proximal AAUAAA polyadenylation signal and the distal AAUAAA polyadenylation signal site are shown flanking the breakpoint in the 3′ UTR. TAA denotes the stop codon in exon 15. (**B**) *MATR3* 3′ RACE products in human control (Lane 1) and DGAP105 lymphoblast (Lanes 2, 3), and control human fetal heart tissue (Lanes 4, 5). RT '+' or '−' denote inclusion or omission of reverse transcriptase in the cDNA synthesis. The large product (1589 bp, arrow) uses the distal polyadenylation signal and predominates in control human lymphoblasts (Lane 1). In contrast, the short product (963 bp, arrow) predominates in DGAP105 lymphoblasts (Lane 2) and in control human fetal heart (Lane 4) and represents *MATR3* transcripts that use the proximal polyadenylation signal. (**C**) Northern blot analysis of adult human tissues shows *MATR3* transcripts of ∼3.5 and ∼2.9 kb. In heart and skeletal muscle, the 2.9-kb transcript predominates and likely corresponds to the 3′ RACE product using the proximal polyadenylation signal. In brain and other tissues, the 3.5-kb transcript predominates and corresponds to the 3′ RACE product using the distal polyadenylation signal. (**D**) Western blot analysis of protein isolated from DGAP105 and three control lymphoblast lines, showing up-regulation of Matrin 3 in DGAP105 compared with controls. Gapdh was used as loading control. (**E**) Quantification of Matrin 3 protein expression in D. Bars represent the mean fold expression of four independent experiments ± SEM, corrected for loading, and normalized to Control 2; *$P < 0.05$ between DGAP105 and mean of the three control lines via paired Student's *t* test.

significant 2.7 ± 0.1-fold (mean ± SEM) up-regulation in Matrin 3 protein levels in DGAP105 cells compared with mean Matrin 3 level in three control lymphoblastoid lines (P<0.05; n = 4 experiments; t-test).

Developmental expression of mouse MATR3 and AHDC1 homologs

To further assess the roles of *MATR3* and *AHDC1* in the DGAP105 heart phenotype, we analyzed the spatial and temporal expression of their mouse homologs in heart, limb and brain at E11.5, E16.5 and newborn stages by semi-quantitative RT–PCR (Fig. 3A). Mouse *Matr3* was strongly expressed in embryonic heart, limb and brain at E11.5 and E16.5 but down-regulated in newborn heart and limb. In contrast, *Ahdc1* expression was present only weakly in E11.5 and E16.5 limb and brain, and either undetectable or expressed at very low levels in developing heart at all stages examined (Fig. 3A). *Ahdc1* expression was readily detected in adult non-cardiac tissues, excluding concerns about detection (data not shown).

To localize *Matr3* expression in the developing heart and to exclude further significant *Ahdc1* expression, we performed section *in situ* hybridization for *Matr3* and *Ahdc1* in mouse embryos at E11.5 (Fig. 3B). These experiments revealed *Matr3* expression in the heart, the CNS, pharyngeal arch mesenchyme and limb bud. In contrast, *Ahdc1* expression was detected only weakly in the embryo and not in the heart. Thus, in contrast to *Ahdc1*, *Matr3* is strongly expressed in the developing mouse heart at developmental times that correlate with genesis of the cardiac abnormalities in DGAP105.

Matrin 3[Gt-ex13] homozygotes are early embryonic lethal

We next prepared *Matr3*[Gt-ex13]-mutant mice (see Materials and Methods, and Fig. 4A) to assess whether the *MATR3* disruption could be causal for the DGAP105 BAV, CoA and PDA phenotypes. Genotype analysis of 14 litters of newborn mice (n = 121) and 12 litters of E8.5–18.5 embryos (n = 92) from *Matr3*[Gt-ex13] heterozygous crosses revealed no homozygotes, indicating a prenatal homozygous lethal phenotype (Table 1). To determine whether *Matr3*[Gt-ex13] homozygotes die before implantation, we collected five litters of E1.5–3.5 embryos (n = 55 total) from heterozygous crosses; homozygous genotypes were detected in only 6 of the 55 embryos (cf. ∼14 expected; P < 0.05, chi-square test) (Table 1). Thus, *Matr3* plays an essential role in early mouse embryonic survival, with significant demise in *Matr3*[Gt-ex13] homozygous embryos occurring before E4.5 and the demise of all remaining embryos occurring between the E4.5 implantation and E8.5 neural fold stages. Proper levels of *Matr3* function are therefore required for embryonic viability both prior to the blastocyst stage and between that time and the neural fold stage.

Functional properties of the Matr3[Gt-ex13] allele

Because early embryonic lethality precluded a cardiac-specific analysis of *Matr3*[Gt-ex13] homozygotes, we turned to *Matr3*[Gt-ex13] heterozygotes. We first sought to determine the mechanism of the *Matr3*[Gt-ex13] mutation (Fig. 4A and B). To do so, we analyzed *Matr3* transcript and Matrin 3 protein expression in wild-type and *Matr3*[Gt-ex13] heterozygotes by 3′ RACE and western blot (Fig. 4C–E).

3′ RACE was performed for mouse *Matr3* using E14.5 heart and brain RNA. Analogous to human *MATR3*, these results confirmed the usage of two AAUAAA signals located 977 and 355 bp downstream of the mouse *Matr3* stop codon. A longer 3′ RACE product of 1647 bp was detected in both tissues, but similar to human, a shorter albeit minor product of 1025 bp was detected only in developing heart RNA (Fig. 4C). Thus, mouse *Matr3* and human *MATR3* are strongly expressed in developing heart, and in both species, there are two distinct polyadenylation signals.

As expected, given the location of the *Matr3*[Gt-ex13] gene trap in exon 13, 5′ to both polyadenylation signals, 3′ RACE showed reductions in the long *Matr3* transcript in *Matr3*[Gt-ex13] heterozygous
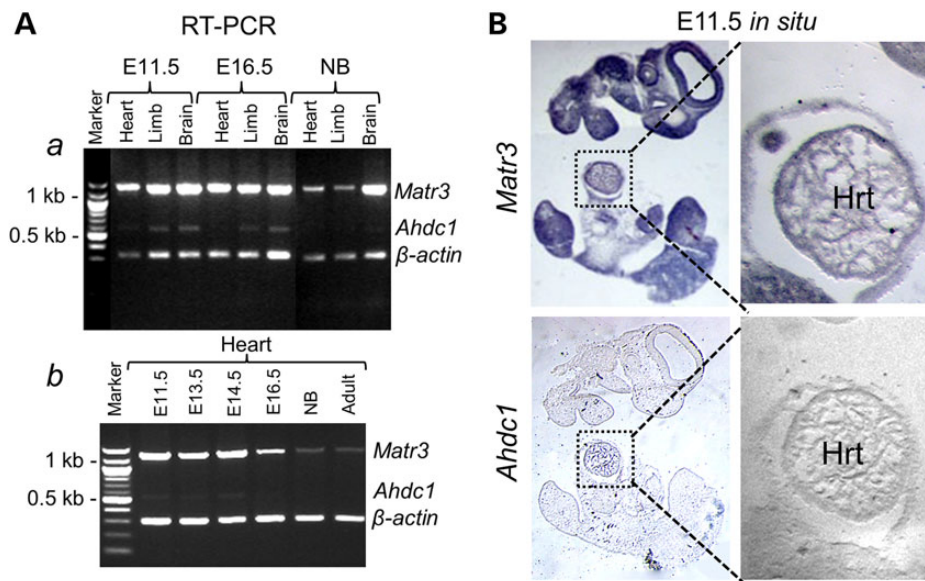

Figure 3. Analysis of mouse *Matr3* and *Ahdc1* transcripts expression in developing heart. (**A**) RT–PCR analyses of *Matr3* and *Ahdc1*. (*a*) Semi-quantitative RT–PCR analyses show strong *Matr3* expression in developing mouse heart, limb and brain at E11.5, 16.5 stages, (*b*) with down-regulation at the newborn (NB) and adult stages. In contrast, *Ahdc1* expression is only weakly detected in limb and brain at E11.5 and 16.5. (**B**) Section *in situ* hybridizations at E11.5 for mouse *Matr3* and *Ahdc1*. *Matr3* is expressed in CNS, pharyngeal arches, limb buds and in the developing heart (enlarged section), whereas *Ahdc1* expression was undetectable in heart (enlarged section). Sense controls (not shown) showed no expression.
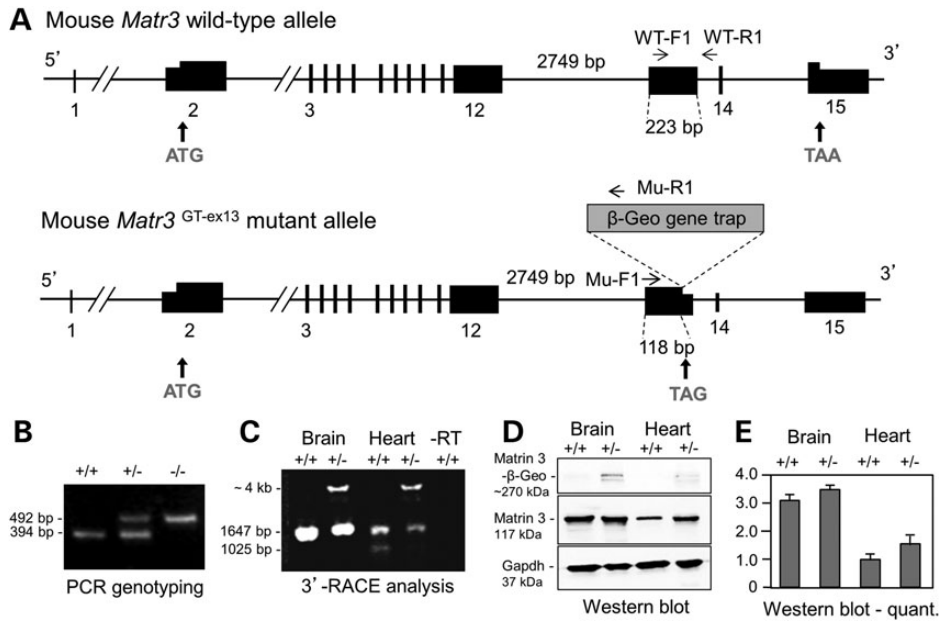
Figure 4. Analysis of the *Matr3*^{Gt-ex13} gene trap allele. (**A**) Structure of mouse *Matr3* wild-type and *Gt-ex13* gene trap mutant alleles. Wild-type mouse *Matr3* encodes an 846-amino acid protein. Intron 12 (2749 bp) and exon 13 (223 bp) are shown. *Matr3*^{Gt-ex-13} gene trap allele inserts a *β-Geo* gene trap vector at position 118 bp in exon 13, which will generate *Matr3-β-geo* fusion transcripts. PCR genotyping primers depict WT-F1 (in exon 13) and WT-R1 (in intron 13) for the wild-type allele, and Mu-F1 (in exon 13) and Mu-R1 (in gene trap vector) for the mutant allele. Primers used in 3′ RACE are summarized on Materials and Methods. (**B**) E3.5 PCR genotyping shows 394-bp wild-type and 492-bp mutant alleles for wild-type (+/+), heterozygous (+/−) and homozygous (−/−) embryos. (**C**) *Matr3*^{GT-ex13} 3′ RACE analysis of mouse E14.5 brain and heart tissues detects a novel *Matr3-β-Geo* fusion transcript (∼4 kb) in heterozygotes. The long *Matr3* 3′ RACE product (1647 bp), the only form detected in brain, is reduced in heterozygous brain. Both long and short *Matr3* 3′ RACE products (1647 and 1025 bp) are reduced in heterozygous heart. (**D**) Western blot analysis of Matrin 3 protein isolated from wild-type and heterozygous mouse E15.5 brain and heart tissues. Gapdh was used as loading control. (**E**) Quantification of Matrin 3 protein expression in D. Bars are fold ± SEM expression level from mean of three independent experiments, corrected for loading, and normalized to a value of 1.0 for wild-type heart. The small increase in expression in *Matr3*^{Gt-ex13/+} heart is not statistically significant.

Table 1. Early embryonic lethality in Matr3^{GT-ex13} homozygous mouse embryos

| | | No. of viable embryos or newborns | | |
Age (total litters)	n	Matr3^{+/+}	Matr3^{GT-ex13/+}	Matr3^{GT-ex13/GT-ex13}
E1.5–4.5 (5)	55	12	37	6^a
E8.5–18.5 (12)	92	22	70	0
Newborn (14)	121	31	90	0

^aNote striking deficiency of *Matr3* homozygous embryos and newborns. The under-representation of homozygotes at E1.5–4.5 is statistically significant ($\chi^2 = 8.56$; $P = 0.014$). Of the six E1.5–4.5 homozygous embryos recovered, three were identified at the blastocyst stage; one, cultured for an additional day, hatched successfully. Additional litters collected between E7.5 and E9.5 contained five dead embryos. These may have represented homozygous embryos that died at or before the E8.5 neural-fold stage.

brain RNA, and in both long and short *Matr3* transcripts in *Matr3*^{Gt-ex13} heterozygous heart RNA (Fig. 4C). However, these analyses also revealed abundant expression of a *Matr3*^{Gt-ex-13/+}-specific ∼4-kb 3′ RACE product corresponding to a β-Geo fusion transcript derived from the gene trap insertion (Fig. 4C). Thus, while interruption of the 3′ end of *Matr3* by the gene trap insertion reduces wild-type transcripts in *Matr3*^{GT-ex13} heterozygotes, this is accompanied by the expression of a fusion transcript that may encode a functional or partly functional Matrin 3-β-Geo fusion protein. Western blot analyses of newborn *Matr3*^{Gt-ex13} heterozygous heart and brain using a Matrin 3-specific antibody failed to detect a statistically significant alteration in Matrin 3 protein levels. However, western blot analysis did reveal the expression of a

Matr3^{Gt-ex13}-specific ∼270-kDa doublet, consistent with the expected Matrin 3-β-Geo fusion protein (Fig. 4D and E).

Cardiac expression of *Matrin 3*

As 3′ RACE and western blot experiments established that Matrin 3-β-Geo fusion transcripts and protein are expressed from the *Matr3*^{GT-ex13} gene trap allele, we sought to use the *β-gal* reporter feature of the *β-geo* gene trap in *Matr3*^{GT-ex13} heterozygotes to more precisely assay endogenous *Matr3* expression. We therefore wished to establish the fidelity of *β-gal* reporter for Matrin 3 at the cellular and subcellular levels. Double-label immunofluorescence for Matrin 3 and β-galactosidase confirmed a high degree of co-localization within E13.5 and E15.5 cardiomyocyte nuclei (Supplementary Material, Fig. S4) and in embryonic kidney and brain (not shown).

We next used X-Gal staining to examine the cardiac expression of the Matrin 3-β-Geo fusion protein in detail. Prominent X-Gal staining was present from E8.5 to term in the developing heart (Fig. 5). Expression starts as early as E8.5 with expression in the right and left ventricular precursors, the bulbus cordis and the common ventricular chamber (Fig. 5B and C). At E11.5, X-Gal staining was present throughout the endocardium and the myocardium (Fig. 5D and E). In newborn mice, X-Gal staining extends throughout all cardiomyocytes in the ventricular, atrial and septal regions (Fig. 5F, and data not shown). We also used Matrin 3 immunochemistry to confirm that Matrin 3 protein is concordantly expressed in the newborn mouse heart (Fig. 6A–C). Immunofluorescent detection showed strong Matrin 3 protein expression in the nuclei of newborn mouse
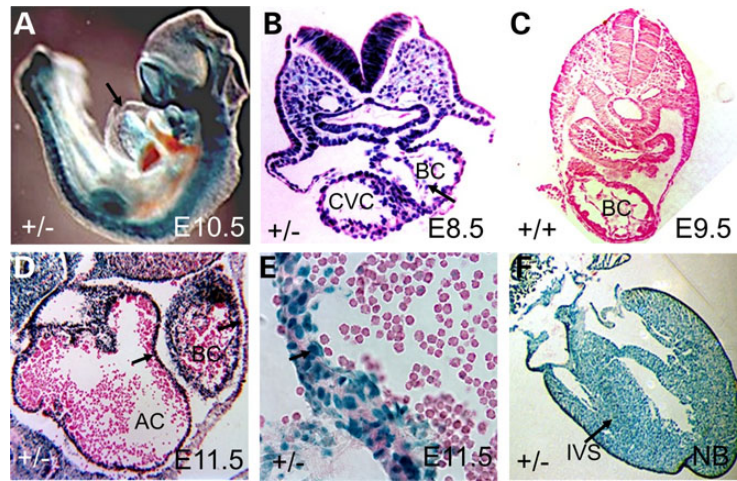
Figure 5. X-Gal staining of *Matr3*^Gt-ex13 heterozygotes. (**A**) X-Gal staining of primitive heart (arrow) in E10.5 *Matr3* heterozygote, and in CNS (brain, spinal cord), pharyngeal arches and limb bud. (**B**) X-Gal staining in primitive heart of E8.5 *Matr3* heterozygote. Arrow depicts dorsal mesocardium; BC, bulbus cordis; CVC, common ventricular chamber. (**C**) Negative control wild-type E9.5 embryo with eosin counterstain. (**D**) X-Gal staining in wall (arrow) of atrial chamber (AC), bulbus cordis (BC) and (**E**) myocardium and endocardium, and (**F**) interventricular septum (IVS) of newborn (NB) *Matr3*^GT-ex13 heterozygote heart (arrows).
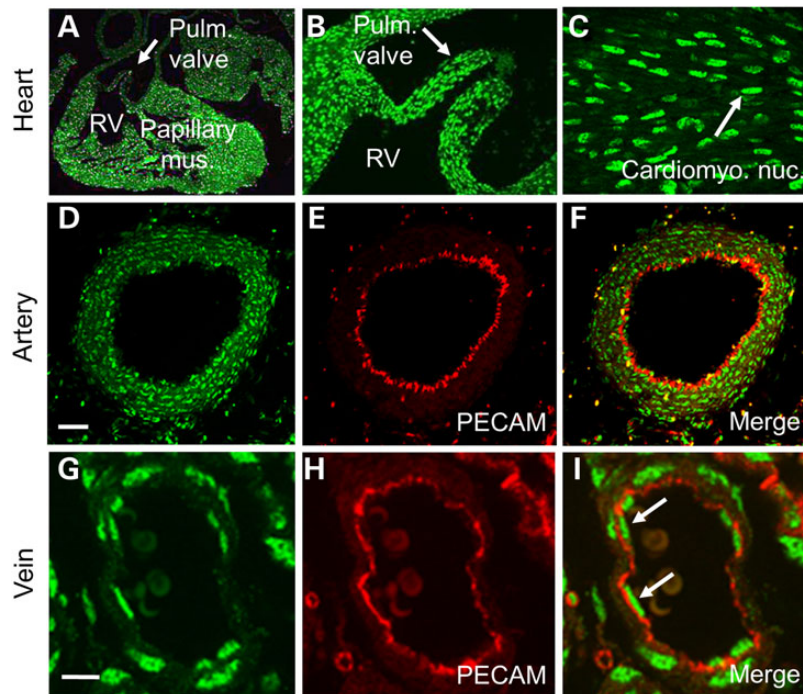

Figure 6. Matrin 3 protein cardiovascular expression in newborn mice. (**A**) Matrin 3 expression in wild-type newborn heart. (**B**) Pulmonary valve (PV) from (A) shows Matrin 3 in interstitial and endocardial cells. (**C**) Matrin 3 in cardiomyocyte nuclei (arrow). (**D–F**) Immunostaining in arterial vascular smooth muscle and endothelial cells for Matrin 3 (D), PECAM (E) and merged (F). Matrin 3 is expressed in both arterial smooth muscle cell nuclei (green) external to PECAM-1 endothelial cell membrane staining (red) and internal to the PECAM-1 domain, in endothelial cell nuclei. This is better seen in (**G–I**) with Matrin 3 and PECAM in small venules, which are largely devoid of vascular smooth muscle. Arrows in (I) denote Matrin 3 in endothelial cell nuclei. Scale bar: 40 μm (D–F); 5 μm (G–I).

ventricular and interventricular septal cardiomyocytes and in the nuclei of cardiac valve interstitial cells and endocardial cells (Fig. 6C).

Matrin 3 is also present in large arterial and venous vascular endothelial cells and in arterial smooth muscle cells as revealed by Matrin 3 and PECAM-1 (platelet-endothelial cell adhesion molecule) double immunostaining (Fig. 6D–I). In large arteries, Matrin 3 is expressed in smooth muscle cell nuclei, external to the expression domain of the endothelial marker PECAM-1 (39); Matrin 3 is also expressed in vascular endothelial cell nuclei, internal to the PECAM-1 expression domain. Endothelial Matrin 3 expression is prominent in large veins, which lack significant smooth muscle (Fig. 6G–I). Thus, in addition to the expression in non-cardiac tissues (Supplementary Material, Fig. S5), Matrin 3 is expressed in developing murine cardiac tissues, including endocardium, endocardial cushions, outflow valves and vascular

endothelium that correspond to the cardiac tissues affected in DGAP105.

Matr3$^{Gt-ex13}$ heterozygotes exhibit subaortic VSD and DORV

Newborn Matr3$^{GT-ex13}$ heterozygotes frequently exhibited abnormal shape and position of the cardiac apex with a characteristic 'boot shape' (Fig. 7A and C, insets). Subsequently, 17 wild-type and 36 heterozygous specimens in 2 different mixed genetic backgrounds (C57BL × 129 and C57BL × FVB) at E16.5, E18.5 and newborn stages were collected and analyzed by histology (Fig. 7, Table 2). No cardiac defects were noted in the wild-type littermates. Of the 36 Matr3$^{Gt-ex13}$ heterozygotes, 11 (30%) exhibited VSDs that were typically subaortic in location (Fig. 7C–F, Table 2). Specifically, in most cases, the aortic valve overrode the right ventricle with 50% or greater overlap and the VSD was closely aligned with the aortic valve, thereby satisfying the definition of DORV with subaortic VSD. In addition, muscular and

subpulmonic VSD phenotypes were also observed (Table 2). The-collective incidence of VSD in Matr3$^{GT-ex13}$ heterozygotes (11 of 36) is statistically significant (P < 0.05; Fisher exact test).

Aortic and outflow valve abnormalities in Matr3$^{Gt-ex13}$ heterozygotes

In addition to VSD, aortic and pulmonary valve defects were also present. BAV was noted in 3 of 26 Matr3$^{GT-ex13}$ heterozygotes (15%), and in 1 case bicuspid pulmonic valve was observed (Fig. 8, Table 2). Although this incidence is not statistically significant, incompletely penetrant BAV phenotypes are also observed in Gata5$^{-/-}$, eNos$^{-/-}$ and Nkx2-5$^{HDneo/+}$ mouse models, and BAV occurs only rarely in wild-type mice (15,16,40). Particularly striking abnormalities were present in the aortic arch and descending aorta, with severe CoA and PDA phenotypes (Fig. 9, Table 2). A total of 43 Matr3$^{GT-ex13}$ newborn heterozygotes were analyzed by corrosion cast analysis after injection of red polymer into the left ventricle, and in some cases, of blue polymer into the
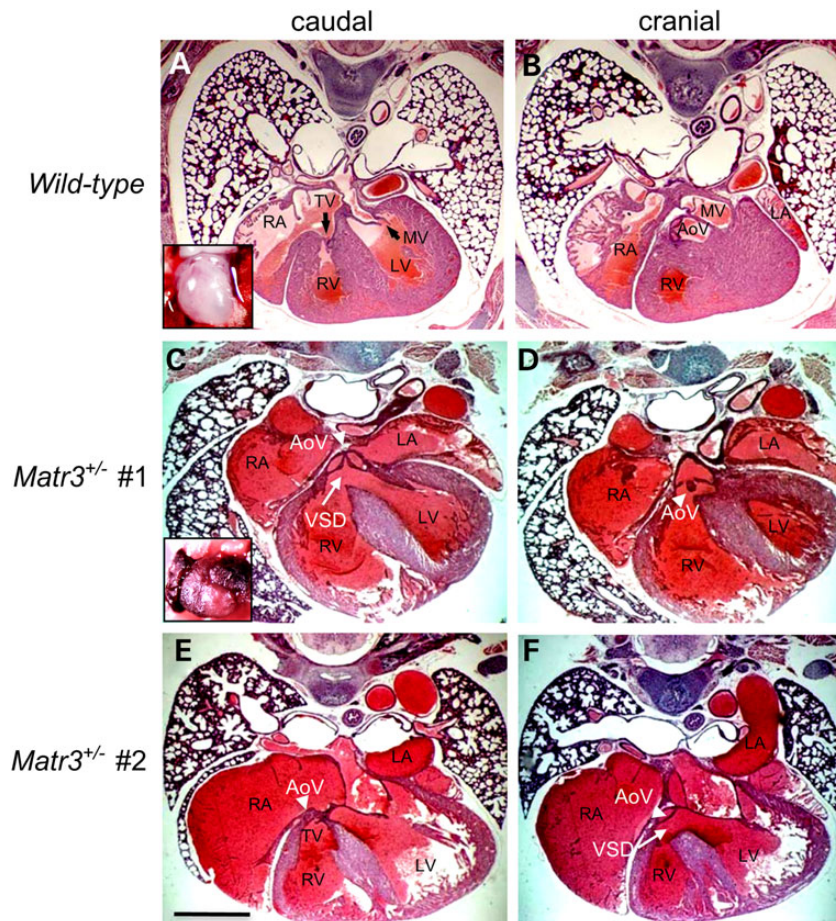

Figure 7. Subaortic VSD and DORV phenotypes in Matr3$^{Gt-ex13}$ heterozygotes. Transverse serial sections through the hearts of E18.5 wild type (**A** and **B**), and two different representative Matr3$^{Gt-ex13}$ heterozygotes (embryo 1 in **C** and **D** and embryo 2 in **E** and **F**), each sectioned at a cranial and caudal level, illustrating the DORV with subaortic VSD phenotype in Matr3$^{Gt-ex13}$ heterozygotes (see Table 2). (A and B) Wild-type sections show left and right ventricles separated by the interventricular septum, the two atrioventricular (tricuspid, mitral) valves and the aortic valve (pulmonic valve not seen in this view). Heterozygous sections do not closely resemble wild-type sections in overall cardiac configuration because, in addition to specific cardiac anomalies, affected newborn Matr3$^{Gt-ex13}$ heterozygote hearts are frequently maloriented and exhibit an abnormal 'boot shape', with the cardiac apex pointing horizontally to the animal's left (see insets, A and C). (C) Subaortic VSD is directly inferior to and aligned with the aortic valve. (D) The aortic valve significantly overrides the right ventricle, which together with the normal communication of right ventricle to pulmonary artery (data not shown), establishes DORV. (E) In this specimen, an unusually close continuity exists between the tricuspid and aortic valves. (F) Subaortic VSD and DORV are shown. AoV, aortic valve; LA and LV, left atrium and ventricle; MV, mitral valve; RA and RV, right atrium and ventricle; TV, tricuspid valve; VSD, ventricular septal defect. Scale bar: 500 μm.

right ventricle. A range of aortic phenotypes was identified, including CoA, IAA and hypoplastic aortic arch (HAA) (overall, 16%). When present, the CoA phenotype occurred at a juxtaductal position, just distal to the left subclavian artery. In addition, a PDA phenotype was noted in 5 of 43 newborn $Matr3^{GT\text{-}ex13}$ heterozygotes (12%), in some cases in association with VSD and IAA, whereas no overt examples of ductus patency were observed in 13 newborn wild-type controls by corrosion cast analysis. The presence of 12 total aortic arch defects including PDA in 43

Table 2. Congenital heart defects in $Matr3^{GT\text{-}ex13}$ embryonic and newborn heterozygotes

Phenotype	$Matr3^{GT\text{-}ex13/+}$ No. affected/ total	$Matr3^{+/+}$ No. affected/ total
1. VSD (histology) (30% penetrance)[a]		
Muscular VSD	1/36	0/17
Membranous VSD	3/36	0/17
DORV with Subaortic VSD	6/36	0/17
DORV with Subpulmonic VSD	1/36	0/17
2. Aortic arch phenotype (corrosion cast) (27% penetrance)[b]		
CoA	3/43	0/13
IAA	2/43	0/13
HAA	2/43	0/13
PDA	5/43	0/13
3. Heart outflow valve phenotype (microdissection) (15% penetrance)		
Bicuspid aortic valve	3/26	0/10
Bicuspid pulmonic valve	1/26	0/10

Analyses were conducted in C57BL/6J × 129/SvJ and C57BL/6J × FVB/N backgrounds. VSD analyses were conducted at E16.5, E18.5 and newborn stages. Aortic arch phenotypes (CoA, PDA) were analyzed at the newborn stage. Although the ductus does not normally close until after birth, we did not observe PDA in controls at this stage by corrosion casting.
[a]Incidence of VSDs in heterozygotes is statistically significant ($P < 0.05$; Fisher exact test).
[b]Although PDAs occurred in mice with IAA (and VSD), the total number of aortic arch defects in heterozygotes is statistically significant ($P < 0.05$; Fisher exact test).

$Matr3^{GT\text{-}ex13}$ newborns is statistically significant ($P < 0.05$; Fisher exact test). Thus, appropriate levels of $Matr3$ function are required for normal cardiac development including formation of the subaortic interventricular septum, morphogenesis of the aorta and, very likely, cuspal development of the aortic and pulmonic valves.

Discussion

AHDC1 haploinsufficiency accounts for impaired cognitive and speech development

The DGAP105 translocation disrupts *MATR3* and *AHDC1* at 5q and 1p breakpoints, respectively. To assign causality for individual components of the proband's phenotype to either or both of these genes, we pursued two approaches: (1) identification of intragenic mutations in independent but phenotypically similar cases and (2) recapitulation of a homologous phenotype by targeted knockout in mouse. For *AHDC1*, a recent report describes *de novo* truncating mutations in four independent subjects with a syndrome defined by intellectual disability, global developmental delay (especially of speech and motor milestones), hypotonia, obstructive sleep apnea, mild facial dysmorphism and mild brain abnormalities by MRI ([38](#)). The co-occurrence of *de novo* truncating mutations in *AHDC1* in four independent cases with concordant phenotypes is *prima facie* evidence for causation of this syndrome by *AHDC1* loss-of-function, with dominant-negative and haploinsufficiency mechanisms suggested as potential explanations for this disorder ([38](#)).

DGAP105 shares a high degree of phenotypic and molecular similarity with the four *AHDC1* truncation index cases. Phenotypes shared in common include impaired intellectual, speech and motor development, facial dysmorphism and respiratory and sleep disturbances. Moreover, cardiac defects were not reported in the four index cases, two of who had normal echocardiograms. In DGAP105, the 1p breakpoint occurs in *AHDC1* intron 1 and would disrupt the 5′ UTR. Furthermore, *AHDC1* expression is reduced to ~50% of wild type in DGAP105 lymphoblastoid cells (Supplementary Material, Fig. S6). Therefore, *AHDC1* haploinsufficiency is the most likely cause of the developmental delay and
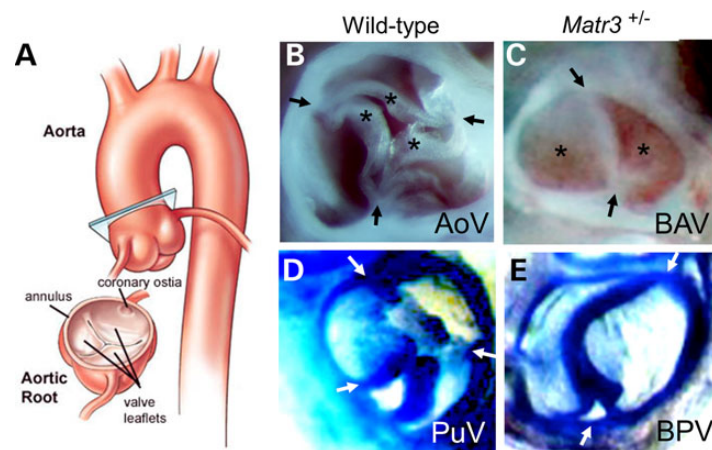

Figure 8. Semilunar heart valve defects in $Matr3^{Gt\text{-}ex\text{-}13}$ heterozygotes. (**A**) Diagram of ascending aorta, aortic arch and descending aorta, showing plane of section for aortic valve analysis. Note left and right coronary ostia (openings) below the fibrous annulus (ring) that demarcates the valve [Cleveland Clinic Foundation (CCF), with permission]. (**B**) Wild-type newborn aortic valve (AoV) showing tri-leaflet (*) morphology in open configuration. Commissural attachments to the annulus are marked (arrows). (**C**) $Matr3^{GT\text{-}ex13}$ heterozygote newborn bicuspid AoV (BAV) showing two leaflets in closed configuration. (**D**) Wild-type newborn pulmonic valve (PuV) showing tri-leaflet morphology in open configuration. (**E**) $Matr3^{GT\text{-}ex13}$ heterozygote newborn bicuspid PuV (BPV) showing two leaflets in closed configuration.
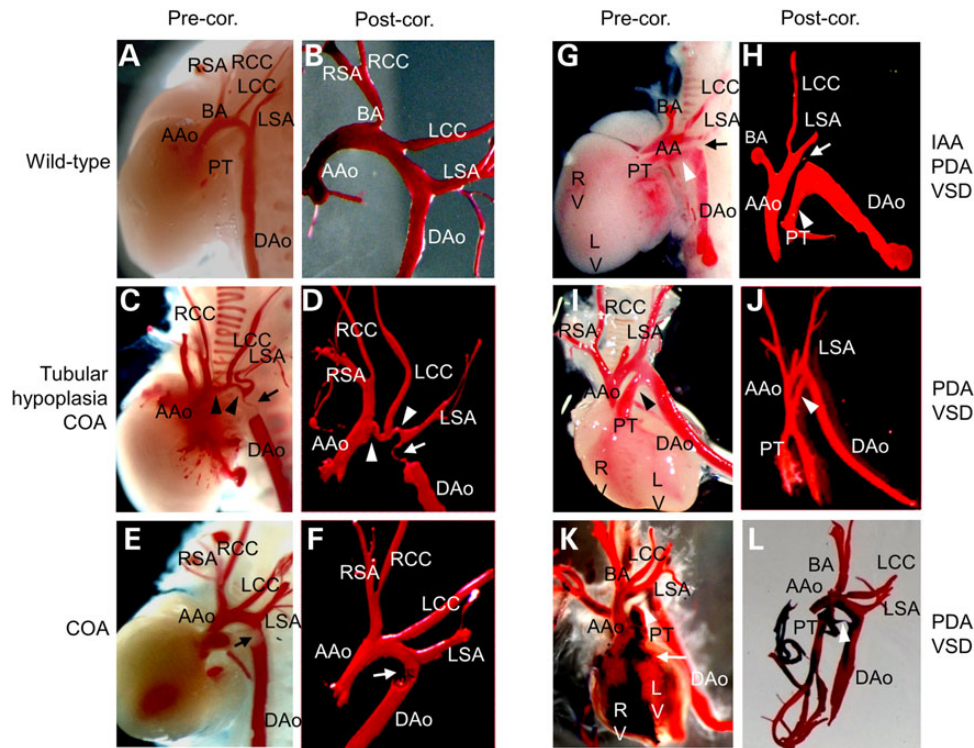
Figure 9. Aortic arch abnormalities in *Matr3*[Gt-ex13] heterozygotes. (**A** and **B**) Newborn wild-type aortic arch vasculature, showing pre- (A) and post-corrosion (B) cast analysis. (**C–L**) *Matr3* heterozygous newborns with various outflow tract defects. (C and D) Tubular hypoplasia and CoA. The deformed aortic arch is uniformly narrowed (segment between arrowheads), and a CoA (arrow) lies distal to the LSA near a closed DAo. (E and F) CoA (arrow) just distal to the LSA and at the level of the closed DAo also called a 'juxaductal CoA'. (G and H) Interrupted aortic arch just distal to the LSA, with a strand of tissue joining the two segments ('atretic aortic arch'; arrow). A VSD with left to right shunting is also present, as evident by red polymer in both ventricles. A large PDA (arrowhead) is the sole source of blood to the lower half of the body. (I and J) A wide PDA (arrowhead) and VSD are present. Following LV injection, both ventricles and the PT contain red polymer; the PT is connected to the PDA that joins the DAo. (K and L) Dual-color corrosion casting shows admixture of red (injected into LV) and blue polymers (injected into RV) in both ventricles, confirming the presence of a VSD (arrow, K). Both polymers are also present in the pulmonary trunk and aorta. A small PDA is present (arrowheads, K and L). AAo, ascending aorta; BA, brachiocephalic artery; DAo, descending aorta; IAA, interrupted aortic arch; LV, left ventricle; PT, pulmonary trunk; RCC/LCC, right/left common carotid arteries; RSA/LSA, right/left subclavian arteries; RV, right ventricle; VSD, ventricular septal defect.

intellectual disability phenotypes in DGAP105 and is unlikely to cause the LVOT defects.

Assignment of human cardiac outflow tract phenotypes to *MATR3* disruption

To confirm our impression that the disruption of *AHDC1* was an unlikely cause of the congenital cardiac disease in DGAP105, we turned to the mouse and assessed expression of *Ahdc1* and *Matr3* during stages of mouse embryonic development that correspond to times at which the relevant developmental timing and tissue interactions for LVOT development occur. *Ahdc1* expression was low or undetectable by RT–PCR and whole-mount *in situ* hybridization in the developing heart and cardiac outflow vessels. In contrast, *Matr3* RNA and protein were both strongly expressed in the developing heart, cardiac outflow tract valves and aorta. Taken with the absence of cardiac phenotypes associated with the previously described *AHDC1* truncation mutations, these results make a major role for *AHDC1* in human or mouse cardiac development unlikely and allowed us to prioritize *Matr3* for gene targeting in mouse.

The presence of distinct embryonic lethal phenotypes in homozygous and LVOT phenotypes in heterozygous *Matr3*[Gt-ex13] mice indicates a sensitive dependence on *Matr3* gene dosage for different developmental processes. Significantly, *Matr3*[Gt-ex13] heterozygotes exhibited incompletely penetrant BAV, CoA and

PDA phenotypes that closely resemble those in DGAP105. We conclude that the cardiac anomalies in *Matr3*[Gt-ex13] heterozygotes result from subtle perturbation in the level or function of *Matr3* transcripts and proteins. In potentially analogous fashion, disruption of the *MATR3* 3′ UTR and slight alterations in Matrin 3 protein levels appear to account for the cardiac findings in DGAP105.

Potential mutational mechanisms involving *MATR3*

In contrast to the *AHDC1* haploinsufficiency observed in DGAP105, a different mutational mechanism for *MATR3* seems to apply that involves subtle alterations in the *MATR3* transcripts and protein levels. We initially anticipated that the disruption of *MATR3* 3′ UTR by the DGAP105 translocation breakpoint should interfere with the proper polyadenylation of *MATR3* transcripts and lead to their destabilization, resulting in loss-of-function. Confounding this simple interpretation, 3′ RACE experiments in human lymphoblasts and fetal heart tissue revealed tissue-specific usage of two different polyadenylation signals, located 362 and 988 bp downstream of the stop codon in exon 15 of *MATR3*. The DGAP105 translocation breakpoint falls at position 667 bp downstream of the stop codon and, therefore, separates the distal but not the proximal polyadenylation signal from the *MATR3* transcription unit. As expected, *MATR3* transcripts in DGAP105 lymphoblasts show a significant but incomplete reduction in

distal polyadenylated transcripts, consistent with residual expression from the wild-type allele.

Interestingly, however, this reduction in longer, distal polyadenylated *MATR3* transcripts is accompanied by up-regulation of shorter proximal polyadenylated transcripts, the form that predominates in fetal heart. As both the longer and shorter transcripts appear to encode the same Matrin 3 protein, and the relative stabilities and translation efficiencies of both transcripts in the developing heart are unknown, the 3′ disruption of *MATR3* could theoretically produce either an up-regulation or a down-regulation of Matrin 3 protein levels. Consistent with the former possibility, western blot analyses revealed a modest but statistically significant up-regulation of Matrin 3 protein of DGAP105 lymphoblasts.

To further clarify the mutational mechanism involved in the *MATR3* disruption in DGAP105, we generated and investigated a mouse *Matr3* gene trap model in which the gene trap insertion in exon 13 toward the 3′ end of mouse *Matr3* approximates the human *MATR3* translocation disruption in exon 15. In this case, owing to its more 5′ location in exon 13, the gene trap insertion results in a reduction in both proximal and distal polyadenylated *Matr3* transcripts. However, in this case, these reductions are accompanied by significant expression of Matrin 3-β-Geo fusion transcript and protein, and the latter largely co-localizes to the same subnuclear domains as endogenous Matrin 3. Although the functional activity of Matrin 3-β-Geo fusion protein relative to wild-type Matrin 3 is unknown, the mouse *Matr3*$^{GT-ex-13}$ allele may act similarly to DGAP105 in producing a net up-regulation of Matrin 3 levels or activity and therefore constitute a gain-of-function state. Because we cannot know Matrin 3 levels or activity in the developing DGAP105 heart, or the activity of the Matrin 3-β-Geo fusion protein in the mouse, we cannot categorically distinguish between gain- and a loss-of-function models for the mouse or human *MATR3* mutations. However, both mutants share disruptions of the 3′ end of *MATR3* that very likely produce subtle alterations in the level of Matrin 3 activity—quantitatively in the case of human *MATR3* as reflected by increased protein levels, or qualitatively in the case of mouse *Matr3*, as reflected by the presence of the Matrin 3-β-Geo fusion protein in embryonic heart. Interestingly, in a *MATR3* sequence analysis of 48 patients with BAV and CoA and in some cases VSD, although no overtly pathogenic coding region mutations (e.g. frameshift or nonsense variants) were observed, we did identify two unique non-coding deletion variants (c.2235-15_16delGT and c.3086_3089delTTAG; NCBI RefSeq: NM_001194955.1). The first variant represents a 2-bp deletion at the −15 and −16 positions in the exon 12 splice acceptor, whereas the second represents a 4-bp deletion in the *MATR3* 3′ UTR. Further experiments are underway to determine whether these variants influence Matrin 3 expression levels.

We attribute the difference in mutational mechanisms for *AHDC1* and *MATR3* to the fact that the DGAP105 translocation breakpoint disrupts the 5′ end of *AHDC1*, in intron 1, but the 3′ end of *MATR3*, in exon 15. It is therefore perhaps not surprising that the DGAP105 translocation breakpoint in *AHDC1* produces a loss-of-function allele, whereas the situation for *MATR3* is significantly more complex, involving subtle alterations in gene and protein expression levels. An attractive molecular model for the latter could involve the loss of distal *MATR3* 3′ UTR microRNA (miR) binding sites. Owing to the absence of miR binding sites that may negatively regulate the translation of distal polyadenylated transcripts, the proximal polyadenylated *MATR3* transcripts might be more efficient in supporting the translation of Matrin 3.

Relation to Matrin 3 S85C mutation

Recently, an autosomal dominant neurological disorder, originally described as 'vocal cord and pharyngeal weakness with distal myopathy', or VCPDM (OMIM #606070), was reclassified as a slowly progressive form of amyotrophic lateral sclerosis, or ALS21 (41–44). VCPDM was originally attributed to a heterozygous S85C missense variant in human Matrin 3 (41,42). However, the mutational mechanism associated with S85C or with other missense variants recently reported in this form of familial ALS remains unclear (44). One clear difference between the S85C VCPDM/ALS phenotype and the cardiac phenotype reported here is that the dominant familial ALS phenotype linked to S85C reflects a missense mutation, whereas the cardiac LVOT phenotypes described here result from 3′ UTR disruptions that affect *MATR3* transcripts that differ at their 3′ ends, thereby influencing protein expression. Thus, the two sets of results are not necessarily inconsistent and appear to reflect distinct functions of *MATR3* in development and disease pathogenesis. We conclude that *MATR3* functions in normal cardiac outflow tract formation and that modest perturbations in Matrin 3 expression in human and mouse are associated with similar LVOTO malformations. Further studies will be required to determine the precise tissue location and nature of the molecular functions attributed to Matrin3 during cardiogenesis.

Materials and Methods

Human genetic analyses

Clinical data
Non-cardiac clinical information for the DGAP105 subject is provided in Supplementary Material under 'DGAP105 clinical history'. Cardiac clinical information is presented in the manuscript under 'Results'. All human studies were conducted under an approved IRB protocol.

Cytogenetics and fluorescence in situ hybridization
Lymphocyte cell transformation was performed at the MGH Center for Human Genetic Research Genomics Core Facility (Boston, MA, USA). DNA samples were prepared from normal individuals (as controls) and from individuals with phenotypes similar to those found in the proband. Metaphase chromosomes were prepared from lymphoblastoid cell lines according to routine protocols. Chromosomes were GTG banded at a resolution of ≥550 bands using standard methods and at least 10 metaphase spreads were examined. The DGAP105 karyotype was initially reported as 46,XY,t(1;5)(p35.3;q31.3)dn by GTG analysis (36), and subsequently revised to 46,XY,t(1;5)(p36.11;q31.2)dn after molecular cytogenetic analysis. BACs for chromosome rearrangement breakpoint mapping were selected using the UCSC Genome Browser and the NCBI Human Genome Browser and labeled directly with either SpectrumOrange- or SpectrumGreen-conjugated dUTP using a nick translation kit (Vysis, Downers Grove, IL, USA). BAC RP11-288L9 and PAC RP1-159A19 were obtained from CHORI (Children's Hospital Oakland Research Institute, Oakland, CA, USA), and BACs CTC-315N8 and CTB-43P18 from Invitrogen (Carlsbad, CA, USA). Metaphase chromosome preparations from DGAP105 were prepared on glass slides following standard hypotonic lysis and fixation, and dehydration in a series of ethanol washes as previously described (45). Array CGH was conducted using an Agilent (Santa Clara, CA, USA) 244K human CGH microarray (~8.9 kb of overall resolution, ~7.4 kb for RefSeq genes).

Breakpoint cloning

Southern blotting was performed by standard methods. BAC sequences from breakpoint critical regions were examined using RepeatMasker to identify regions from which unique probes could be generated. Genomic DNAs were digested with *Dra*I, *Eco*RI, *Hind*III, *Rsa*I, *Sca*I and probed with a 505-bp fragment amplified from RP1-159A19. Rearrangement breakpoints were cloned using modifications of the suppression PCR protocol (45). Cloned junction fragments were sequenced by standard methods.

3′ rapid amplification of cDNA ends (3′ RACE) analysis (human and mouse)

3′ rapid amplification of cDNA ends (3′ RACE) on human and mouse RNA samples was performed according to the SMARTer RACE 5′/3′ kit protocol (Clontech, Cat # 634858). Briefly, 2.5 ul cDNA samples that were prepared by the SMARTScribe Reverse Transcriptase (Clontech) from the total RNA samples isolated from the lymphoblast cells of patient DGAP 105, controls and normal human fetal heart tissues, as well as the heart and brain tissues from E14.5 embryos of *Matr3*[GT-ex13] heterozygous and wild-type mice using NucleoSpin (Clontech) according to the manufacturer's instructions. Following gene-specific forward primers (GSPs) for human *MATR3* and mouse *Matr3* genes together with common Universal Reverse Primer (UPM) were used in the 3′ RACE PCR. hMATR3-GSP-F1: 5′ GCAGCAGCACTGCTAGAAAGTGGCA 3′; mMatr3-GSP-F1: 5′ GACCAGACAGAACAGGAGCCCAGCA 3′; 3′ RACE-UPM: 5′ TAATACGACTCACTATAGGGCAAGCAGTGGTATCAACGCAGAGT 3′.

PCR were performed in following condition: 30 s at 94°C, 30 s at 68°C, followed by 3 min at 72°C for 25 cycles. PCR products were analyzed by agarose gel electrophoresis and digested by specific restriction enzymes. The large and small 3′ RACE PCR products were purified from the agarose gel and the sequenced by Sanger sequencing.

Northern blot analysis

A northern blot containing human tissue polyA+ RNA (Clontech, Mountain View, CA, USA) was hybridized with a probe corresponding to exons 13–14 of *MATR3*. Random-primed probe labeling was performed with the MegaPrime labeling kit (GE Healthcare, Piscataway, NJ, USA), according to the manufacturer's instructions.

Quantitative real-time RT–PCR (human and mouse)

For quantitative real-time RT–PCR, Taqman assays were employed for human *MATR3* and mouse *Matr3* transcripts. Total RNA was extracted from lymphoblastoid cell lines and mouse tissues using NucleoSpin kit (Clontech) according to the manufacturer's instructions. Purified RNA samples were reverse transcribed using the qScript dDNA SuperMix (Quanta). Each cDNA sample was then subjected to Taqman real-time PCR analysis on a 7500 FAST real-time PCR system (Life Technologies): Human *MATR3* TaqMan assay (Assay ID:Hs00251579_m1), Mouse *Matr3* TaqMan assay (Assay ID: Mm00726619_s1, in exon 2) and Mouse *Matr3* TaqMan assay (Assay ID: Mm01704913_g1 in exon 15). *Gapdh* expression was used as an endogenous control. Relative gene expression was analyzed using comparative C_T methods (46). The PCR reaction consisted of 10 μl of Master Mix 2× concentrate. All assays were performed in triplicate.

For *AHDC1*, a SYBR green assay was employed. Total RNA was extracted from lymphoblastoid cell lines using TRIZOL reagent (Invitrogen) according to the manufacturer's instructions. RNA quality was assessed by gel electrophoresis and spectrophotometric measurement of OD 260/280. Purified RNA samples were reverse transcribed using the AccuScriptTM High Fidelity 1st

Strand cDNA Synthesis kit (Stratagene, La Jolla, CA, USA) according to the manufacturer's instructions. Real-time PCR was performed using the LightCycler® 480 SYBR Green I Master Kit (Roche, Nutley, NJ, USA), on a LightCycler® 480 Real Time PCR System (Roche). The PCR reaction consisted of 10 μl of Master Mix 2× concentrate, 0.35 μM of each forward and reverse primer, template cDNA and PCR grade water to a final volume of 20 μl in the LightCycler 480 96-well plate. An initial denaturation step at 95 °C for 10 min was followed by 40 cycles of 95°C for 10 s, 60°C for 20 s and 72°C for 10 s. A single fluorescence measurement was conducted at the end of the 72°C extension segment. After amplification, melting curve analysis was performed by heating the sample to 95°C for 5 s, then cooling it to 65°C for 1 min, followed by a linear temperature increase to 95°C at a rate of 0.11°C/s, while continuously monitoring the fluorescent signal. All primer sets were confirmed by agarose gel electrophoresis to produce a single band of expected size that had the expected melting curve. Data analysis was performed with LightCycler® 480 Relative Quantification software (Roche) (46). Multiple primer sets were selected for *AHDC1* to enable analysis of transcripts from either the wild-type allele only (by designing primer pairs that flank the breakpoint), e.g. *AHDC1* exons 1–2 flanking the intron 1 site of the breakpoint CTCCACGACTCCTCTCCTCA + AATCAGGCAAGCTCCCATC; or from wild-type plus translocated alleles, e.g. *AHDC1* exon 3: ACCTGAGAGAACTGGGAGGAG + TCCACAGACTCCGGTAGAGAG; *AHDC1* exon 6: GAGTCATCCTCCGACAGCAC + GTCCATCATCAGTTTCTCCA. *B2M* (β2 microglobulin: CGTCATCCAGCAGAGA + GACAAGTCTGAATGCTCC) was used as an internal control for normalization. All assays were performed in triplicate and included marker-positive and marker-negative controls and reagent with no template controls.

Western blot analyses (human and mouse)

For human Matrin 3 analyses, lymphoblastoid cell lines were grown in suspension in T25 flasks in RPMI 1640 culture medium supplemented with 10% FBS, 1% Pen/Strep and 1% L-glutamine. For suspension human lymphoblast cells, RIPA buffer was added after the cell pellets were washed with 1× cold PBS. Cells were disrupted by repeated aspiration through a 21-gauge needle. Mouse heart or brain tissues from E14.5 embryos were homogenized with RIPA buffer on ice. Samples were centrifuged for 10 min at 4°C. For western blots, 40 μg of protein was diluted with 2× protein-loading buffer to 1× final concentration and heated at 95°C for 10 min. Proteins were resolved on NuPAGE 4–12% Bis-Tris Gel (Life Technologies). Western blots were treated with a rabbit anti-Matrin 3 antibody (Cat. no. ab70336, Abcam). This Matrin 3 antibody recognizes a region between residue 475 and 500 of human Matrin 3. Protein loading controls were detected with an anti-Gapdh antibody from Millipore. Band intensity was quantified using ImageJ.

For mouse Matrin 3 analyses, total protein from newborn *Matr3*[Gt-ex13] mouse tissues was isolated using a NEP3229 Barocycler (Pressure BioSciences, West Bridgewater, MA, USA) according to the manufacturer's standard protocol. For western blots, 40 μg of protein was diluted with 6× protein loading buffer to 1× final concentration and heated at 95°C for 20 min. Proteins were resolved on 8% SDS–PAGE. Western blots employed a rabbit anti-Matrin 3 antibody (Cat. no. ab70336, Abcam; cat. no. A300-591A, Bethyl Laboratories, Montgomery, TX, USA). This Matrin 3 antibody recognizes a region between residue 800 and the C-terminus (residue 847) of human Matrin 3.

Mutation screening

As noted, because of phenotypic overlap between DGAP105 and NS, we screened DGAP105 for exonic mutations in *PTPN11*,

KRAS and *SOS1*, with negative results. In addition, 132 individuals with a clinical diagnosis of NS who were negative for mutations *PTPN11* and *KRAS* were screened comprehensively for mutations in the coding regions and exon–intron boundaries of *MATR3* and *AHDC1* by bi-directional sequence analysis. No overt pathogenic mutation was identified, indicating that mutations of *MATR3* and *AHDC1* are unlikely to account for any significant proportion of NS. In addition, we performed bi-directional sequence analysis of all 15 *MATR3* exons including splice junctions in a collection of DNAs (Boston Children's Hospital) obtained from 48 individuals with BAV and CoA and in some cases VSD (see Discussion).

Mouse molecular genetics

Generation of Matr3$^{Gt-ex13}$ gene trap mice

A βgeo gene trap mouse embryonic stem (mES) cell line (RRR075, strain Ola/129) was identified in the BayGenomics database (now part of the International Gene Trap Consortium). By long-range PCR and DNA sequence analysis, the location of the pGTOLxf gene trap insertion site was determined and found to reside within *Matr3* exon 13 (Fig. 4). These ES cells were injected into blastocysts to generate chimeras, and germline transmission was obtained. Most *Matr3* offspring heterozygous for this gene trap insertion were viable and fertile. In accord with gene trap nomenclature rules (47), we have designated this mutant allele Matr3$^{Gt(pGTOLxf)ex13Rlm}$, in which Gt designates 'gene trap', *pGTOLxf* the gene trap vector, Rlm the laboratory ILAR code, and ex13 replaces the lab serial number to reflect the gene trap integration site within exon 13. For convenience, we have further designated this allele as *Matr3*$^{Gt-ex13}$.

For *Matr3* mouse genotyping, the wild-type allele was amplified with forward primer Matr3-wtF1 (5′ GGGTGCCGAATCTGCTG AGAAT 3′) and reverse primer Matr3-wtR1 (5′ CCAACAATATCAC ATTACCCTTTTG 3′). The mutant Matr3$^{Gt-ex13}$ allele was amplified by forward primer Matr3-muF1 (5′ GTGGACAAGATTGAGGAA CTTGA 3′) and reverse primer Matr3-muR1 (5′ TGAGATGGA TTGGCAGATGTAGC 3′). All mice were maintained in either a C57BL/6J × 129/SvJ or in a C57BL/6J × FVB/N mixed background and housed in a pathogen-free barrier facility. Mouse work was approved by the Harvard Medical School IACUC. *Matr3*$^{Gt-ex13/+}$ mice are available upon request.

Analysis of E1.5–4.5 Matr3$^{Gt-ex13}$ homozygous embryos

Pregnant female mice were sacrificed and E1.5–4.5 embryos isolated by flushing the Fallopian tube with M2 medium (cat. no. M7167, Sigma), using a 27-gauge needle attached to a 1-ml syringe. Individual embryos were isolated with a glass micropipette and transferred to separate microfuge tubes. Lysis buffer (3 μl of 0.05% SDS, 0.035 N NaOH) was added to each tube and boiled for 3 min at 95°C. Three microliters of embryonic DNA was split between wild-type and mutant allele genotyping reactions (45 cycles of PCR), followed by agarose gel electrophoresis.

Immunohistochemical analyses

Immunohistochemistry was performed with rabbit anti-Matrin 3 antibody (cat. no. IHC-00081, Bethyl Laboratories), PECAM-1 antibody at 1 : 50 dilution (BD Pharmingen, San Jose, CA, USA) and chicken anti-beta Galatosidase antibody (cat. no. ab9361, Abcam). Antibody reactions on OCT-embedded sections were visualized by secondary antibody conjugated with FITC or Cy3 and Alexa Fluor® 594-AffiniPure goat anti-chick for immunofluorescence staining, or using the Vectastain ABC kit (Vector Labs, Burlingame, CA, USA) for immunoperoxidase staining. Hematoxylin

and Eosin staining and histological analyses were performed using standard procedures.

X-Gal staining and whole-mount in situ hybridization

X-Gal staining to detect β-galactosidase activity was performed according to standard protocols. Briefly, embryos were fixed for 30–90 min in fixative consisting of 1% formaldehyde and 0.2% gluteraldehyde in PBS. Whole-mount or OCT-embedded frozen sections were stained with a solution containing 1 mg/ml X-Gal for 3–6 h. Whole-mount *in situ* hybridization experiments were performed as previously described (48) using a *Matr3* 1.3-kb anti-sense and Ahdc1 564-bp anti-sense probes.

Vascular analyses by corrosion casting

Newborn *Matr3*$^{Gt-ex13}$ heterozygotes and wild-type littermate controls were anesthetized with Avertin and the heart exposed by thoracic incision and rib removal. Batson no. 17 methacrylate plastic (cat. No. 07349, Polysciences, Inc., Warrington, PA, USA) was injected into the beating left ventricle after inclusion of red pigment (for arterial analysis) or into the right ventricle with blue pigment (for venous) analysis, according to the manufacturer's instructions. After hardening, tissue was removed with maceration solution (Polysciences) at 50°C for 72 h, and the resulting corrosion casts were photographed. Outflow tract cardiac valve morphology was assessed by microdissection, in some cases after light staining with Toluidine blue.

Note Added in Proof

The *AHDC1* disruption described here has now been assigned as OMIM #615829, Xia-Gibbs Syndrome.

Supplementary Material

Supplementary Material is available at *HMG* online.

Web Resources

BayGenomics database (now part of International Gene Trap Consortium: http://www.genetrap.org/)
Developmental Genome Anatomy Project (DGAP) (http://www.bwhpathology.org/dgap/)
Ensembl (http://www.ensembl.org/Homo_sapiens/)
Eppig and Levan, 2007 (http://www.informatics.jax.org/mgihome/nomen/gene.shtml#gtl)
NCBI Human Genome Browser (http://www.ncbi.nlm.nih.gov/)
Repeat Masker (http://www.repeatmasker.org)
UCSC Genome Browser (http://genome.ucsc.edu)

References

1. Andersen, T.A., Troelsen Kde, L. and Larsen, L.A. (2014) Of mice and men: molecular genetics of congenital heart disease. *Cell. Mol. Life Sci.*, **71**, 1327–1352.
2. Lalani, S.R. and Belmont, J.W. (2014) Genetic basis of congenital cardiovascular malformations. *Eur. J. Med. Genet.*, **57**, 402–413.
3. Jenkins, K.J., Correa, A., Feinstein, J.A., Botto, L., Britt, A.E., Daniels, S.R., Elixson, M., Warnes, C.A. and Webb, C.L. (2007) Noninherited risk factors and congenital cardiovascular defects: current knowledge: a scientific statement from the American Heart Association Council on Cardiovascular Disease in the Young: endorsed by the American Academy of Pediatrics. *Circulation*, **115**, 2995–3014.
4. Pierpont, M.E., Basson, C.T., Benson, D.W. Jr, Gelb, B.D., Giglia, T.M., Goldmuntz, E., McGee, G., Sable, C.A., Srivastava, D. and Webb, C.L. (2007) Genetic basis for congenital heart defects: current knowledge: a scientific statement from the American Heart Association Congenital Cardiac Defects Committee, Council on Cardiovascular Disease in the Young: endorsed by the American Academy of Pediatrics. *Circulation*, **115**, 3015–3028.
5. Siu, S.C. and Silversides, C.K. (2010) Bicuspid aortic valve disease. *J. Am. Coll. Cardiol.*, **55**, 2789–2800.
6. Braverman, A.C., Güven, H., Beardslee, M.A., Makan, M., Kates, A.M. and Moon, M.R. (2005) The bicuspid aortic valve. *Curr. Probl. Cardiol.*, **30**, 470–522.
7. Verma, S. and Siu, S.C. (2014) Aortic dilatation in patients with bicuspid aortic valve. *N. Engl. J. Med.*, **370**, 1920–1929.
8. Kenny, D. and Hijazi, Z.M. (2011) Coarctation of the aorta: from fetal life to adulthood. *Cardiology J.*, **18**, 487–495.
9. Lalani, S.R., Shaw, C., Wang, X., Patel, A., Patterson, L.W., Kolodziejska, K., Szafranski, P., Ou, Z., Tian, Q., Kang, S.H. et al. (2013) Rare DNA copy number variants in cardiovascular malformations with extracardiac abnormalities. *Eur. J. Hum. Genet.*, **21**, 173–181.
10. Zaidi, S., Choi, M., Wakimoto, H., Ma, L., Jiang, J., Overton, J.D., Romano-Adesman, A., Bjornson, R.D., Breitbart, R.E., Brown, K.K. et al. (2013) De novo mutations in histone-modifying genes in congenital heart disease. *Nature*, **498**, 220–223.
11. Garg, V., Muth, A.N., Ransom, J.F., Schluterman, M.K., Barnes, R., King, I.N., Grossfeld, P.D. and Srivastava, D. (2005) Mutations in NOTCH1 cause aortic valve disease. *Nature*, **437**, 270–274.
12. McBride, K.L., Riley, M.F., Zender, G.A., Fitzgerald-Butt, S.M., Towbin, J.A., Belmont, J.W. and Cole, S.E. (2008) NOTCH1 mutations in individuals with left ventricular outflow tract malformations reduce ligand-induced signaling. *Hum. Mol. Genet.*, **17**, 2886–2893.
13. Riley, M.F., McBride, K.L. and Cole, S.E. (2011) NOTCH1 missense alleles associated with left ventricular outflow tract defects exhibit impaired receptor processing and defective EMT. *Biochim. Biophys. Acta*, **1812**, 121–129.
14. de la Pompa, J.L. and Epstein, J.A. (2012) Coordinating tissue interactions: Notch signaling in cardiac development and disease. *Dev. Cell*, **22**, 244–254.
15. Lee, T.C., Zhao, Y.D., Courtman, D.W. and Stewart, D.J. (2000) Abnormal aortic valve development in mice lacking endothelial nitric oxide synthase. *Circulation*, **101**, 2345–2348.
16. Laforest, B., Andelfinger, G. and Nemer, M. (2011) Loss of Gata5 in mice leads to bicuspid aortic valve. *J. Clin. Invest.*, **121**, 2876–2887.
17. Padang, R., Bagnall, R.D., Richmond, D.R., Bannon, P.G. and Semsarian, C. (2012) Rare non-synonymous variations in the transcriptional activation domains of GATA5 in bicuspid aortic valve disease. *J. Mol. Cell. Cardiol.*, **53**, 277–281.
18. Bonachea, E.M., Chang, S.W., Zender, G., Lahaye, S., Fitzgerald-Butt, S., McBride, K.L. and Garg, V. (2014) Rare GATA5 sequence variants identified in individuals with bicuspid aortic valve. *Pediatr. Res.*, **76**, 211–216.
19. Laforest, B. and Nemer, M. (2011) GATA5 interacts with GATA4 and GATA6 in outflow tract development. *Dev. Biol.*, **358**, 368–378.
20. Katz, S.G., Williams, A., Yang, J., Fujiwara, Y., Tsang, A.P., Epstein, J.A. and Orkin, S.H. (2003) Endothelial lineage-mediated loss of the GATA cofactor friend of GATA 1 impairs cardiac development. *Proc. Natl Acad. Sci. USA.*, **100**, 14030–14035.
21. Nadeau, M., Georges, R.O., Laforest, B., Yamak, A., Lefebvre, C., Beauregard, J., Paradis, P., Bruneau, B.G., Andelfinger, G. and Nemer, M. (2010) An endocardial pathway involving Tbx5, Gata4, and Nos3 required for atrial septum formation. *Proc. Natl Acad. Sci. USA*, **107**, 19356–19361.
22. McBride, K.L., Zender, G.A., Fitzgerald-Butt, S.M., Seagraves, N.J., Fernbach, S.D., Zapata, G., Lewin, M., Towbin, J.A. and Belmont, J.W. (2011) Association of common variants in ERBB4 with congenital left ventricular outflow tract obstruction defects. *Birth Defects Res. A Clin. Mol. Teratol.*, **91**, 162–168.
23. Gitler, A.D., Lu, M.M. and Epstein, J.A. (2004) PlexinD1 and semaphorin signaling are required in endothelial cells for cardiovascular development. *Dev. Cell.*, **7**, 107–116.
24. Kaartinen, V., Dudas, M., Nagy, A., Sridurongrit, S., Lu, M.M. and Epstein, J.A. (2004) Cardiac outflow tract defects in mice lacking ALK2 in neural crest cells. *Development*, **131**, 3481–3490.
25. Thomas, P.S., Sridurongrit, S., Ruiz-Lozano, P. and Kaartinen, V. (2012) Deficient signaling via Alk2 (Acvr1) leads to bicuspid aortic valve development. *PLoS ONE*, **7**, e35539.
26. Guo, C., Sun, Y., Zhou, B., Adam, R.M., Li, X., Pu, W.T., Morrow, B.E., Moon, A. and Li, X. (2011) A Tbx1-Six1/Eya1-Fgf8 genetic pathway controls mammalian cardiovascular and craniofacial morphogenesis. *J. Clin. Invest.*, **121**, 1585–1595.
27. Caprio, C. and Baldini, A. (2014) p53 suppression partially rescues the mutant phenotype in mouse models of DiGeorge syndrome. *Proc. Natl Acad. Sci. USA*, **111**, 13385–13390.
28. Jain, R., Engleka, K.A., Rentschler, S.L., Manderfield, L.J., Li, L., Yuan, L. and Epstein, J.A. (2011) Cardiac neural crest orchestrates remodeling and functional maturation of mouse semilunar valves. *J. Clin. Invest.*, **121**, 422–430.
29. Peterson, R.T., Shaw, S.Y., Peterson, T.A., Milan, D.J., Zhong, T.P., Schreiber, S.L., MacRae, C.A. and Fishman, M.C. (2004) Chemical suppression of a genetic mutation in a zebrafish model of coarctation. *Nat. Biotech.*, **22**, 595–599.

30. Tagariello, A., Breuer, C., Birkner, Y., Schmidt, S., Koch, A.M., Cesnjevar, R., Ruffer, A., Dittrich, S., Schneider, H., Winterpacht, A. *et al.* (2012) Functional null mutations in the gonosomal homologue gene *TBL1Y* are associated with non-syndromic coarctation of the aorta. *Curr. Mol. Med.*, **12**, 199–205.

31. Lalani, S.R., Ware, S.M., Wang, X., Zapata, G., Tian, Q., Franco, L.M., Jiang, Z., Bucasas, K., Scott, D.A., Campeau, P.M. *et al.* (2013) MCTP2 is a dosage-sensitive gene required for cardiac outflow tract development. *Hum. Mol. Genet.*, **22**, 4339–4348.

32. Hajj, H. and Dagle, J.M. (2012) Genetics of patent ductus arteriosus susceptibility and treatment. *Semin. Perinatol.*, **36**, 98–104.

33. Satoda, M., Zhao, F., Diaz, G.A., Burn, J., Goodship, J., Davidson, H.R., Pierpont, M.E. and Gelb, B.D. (2000) Mutations in TFAP2B cause Char syndrome, a familial form of patent ductus arteriosus. *Nat. Genet.*, **25**, 42–46.

34. Zhao, F., Weismann, C.G., Satoda, M., Pierpont, M.E., Sweeney, E., Thompson, E.M. and Gelb, B.D. (2001) Novel TFAP2B mutations that cause Char syndrome provide a genotype-phenotype correlation. *Am. J. Hum. Genet.*, **69**, 695–703.

35. Zhao, F., Bosserhoff, A.-K., Buettner, R. and Moser, M. (2011) A heart-hand syndrome gene: Tfap2b plays a critical role in the development and remodeling of mouse ductus arteriosus and limb patterning. *PLoS ONE*, **6**, e22908.

36. Higgins, A.W., Alkuraya, F.S., Bosco, A.F., Brown, K.K., Bruns, G.A.P., Donovan, D.J., Eisenman, R., Fan, Y., Farra, C.G., Ferguson, H.L. *et al.* (2008) Characterization of apparently balanced chromosomal rearrangements from the developmental genome anatomy project. *Am. J. Hum. Genet.*, **82**, 712–722.

37. Roberts, A.E., Allanson, J.E., Tartaglia, M. and Gelb, B.D. (2013) Noonan syndrome. *Lancet*, **381**, 333–342.

38. Xia, F., Bainbridge, M.N., Tan, T.Y., Wangler, M.F., Scheuerle, A.E., Zackai, E.H., Harr, M.H., Sutton, V.R., Nalam, R.L., Zhu, W. *et al.* (2014) *De Novo* truncating mutations in AHDC1 in individuals with syndromic expressive language delay, hypotonia, and sleep apnea. *Am. J. Hum. Genet.*, **94**, 784–789.

39. Ayalon, O., Sabanai, H., Lampugnani, M.G., Dejana, E. and Geiger, B. (1994) Spatial and temporal relationships between cadherins and PECAM-1 in cell-cell junctions of human endothelial cells. *J. Cell Biol.*, **126**, 247–258.

40. Biben, C., Weber, R., Kesteven, S., Stanley, E., McDonald, L., Elliott, D.A., Barnett, L., Köentgen, F., Robb, L., Feneley, M. and Harvey, R.P. (2000) Cardiac septal and valvular dysmorphogenesis in mice heterozygous for mutations in the homeobox gene *Nkx2–5*. *Circ. Res.*, **87**, 888–895.

41. Feit, H., Silbergleit, A., Schneider, L.B., Gutierrez, J.A., Fitoussi, R.P., Réyès, C., Rouleau, G.A., Brais, B., Jackson, C.E., Beckmann, J.S. *et al.* (1998) Vocal cord and pharyngeal weakness with autosomal dominant distal myopathy: clinical description and gene localization to 5q31. *Am. J. Hum. Genet.*, **63**, 1732–1742.

42. Senderek, J., Garvey, S.M., Krieger, M., Guergueltcheva, V., Urtizberea, A., Roos, A., Elbracht, M., Stendel, C., Tournev, I., Mihailova, V. *et al.* (2009) Autosomal dominant distal myopathy associated with a recurrent missense mutation in the gene encoding the nuclear matrix protein, Matrin 3. *Am. J. Hum. Genet.*, **84**, 511–518.

43. Kraya, T. and Zierz, S. (2013) Distal myopathies: from clinical classification to molecular understanding. *J. Neural Transm.*, **120**(Suppl 1), S3–S7.

44. Johnson, J.O., Pioro, E.P., Boehringer, A., Chia, R., Feit, H., Renton, A.E., Pliner, H.A., Abramzon, Y., Marangi, G., Winborn, B.J. *et al.* (2014) Mutations in the Matrin 3 gene cause familial amyotrophic lateral sclerosis. *Nat. Neurosci.*, **17**, 664–666.

45. Siebert, P.D., Chenchik, A., Kellogg, D.E., Lukyanov, K.A. and Lukyanov, S.A. (1995) An improved PCR method for walking in uncloned genomic DNA. *Nucl. Acids Res.*, **23**, 1087–1088.

46. Schmittgen, T.D. and Livak, K.J. (2008) Analyzing real-time PCR data by the comparative C(T) method. *Nat. Protoc.*, **3**, 1101–1108.

47. Eppig, J.T. and Levan, G. (2007) MGI_4.0 - Rules for Nomenclature of Genes, Genetic Markers, Alleles, and Mutations in Mouse and Rat.

48. Xu, P.X., Woo, I., Her, H., Beier, D.R. and Maas, R.L. (1997) Mouse Eya homologues of the Drosophila eyes absent gene require Pax6 for expression in lens and nasal placode. *Development*, **124**, 219–231.